Chapter 2

Experimental setup

The current experiments are designed to examine the effect of volume fraction and Stokes number (and equivalently the Reynolds number) at shear rates sufficiently high enough so that particle interactions are expected to become important. Neutrally buoyant and settling particles are used (ρ_p/ρ from 1 to 1.4). In this chapter the rheometer and the method used for making the torque measurements are described (Section 2.1). Subsequently, the particles and the interstitial liquids that were employed to create the liquid-solid mixtures are reported in Section 2.2. Finally, the modification of the experimental apparatus for making visualizations of the flow and its procedure is specified in Section 2.6.

2.1 Rheometer

In Figure 2.1 a schematic of the concentric-cylinder rheometer is shown. The rheometer is designed to measure the shear stress of liquid-solid mixtures that feature relatively large particles (the order of mm size) and are sheared at considerably shear rates. One of the difficulties that arises with high shear rates flows is the presence of secondary flows. As shown by the review of Hunt et al. (2002), an improper design of an experiment can result in observations that do not reflect the behavior of the particulate flow itself. For this reason, the rheometer is designed to delay the presence of secondary flows (Taylor vortices). This is the same experimental apparatus used by Koos (2009). It consists of a rotational outer cylinder and an inner cylinder that consists of three parts: the top and bottom static cylinders (fixed guard cylinders), and the middle cylinder (test cylinder) which is instrumented to make measurements of the torque. The concentric and rotating outer cylinders are all made of stainless steel.

The liquid-solid mixture is sheared by the rotation of the outer drum and the torque measurements take place at the test cylinder. This cylinder is supported by a central shaft, which, in turn, has ball bearings mounted to allow the free deflection of this cylinder. A set of ball bearings is also located between the rotating outer cylinder and the fixed guard cylinders to reduce friction. The

Particles
and liquid
inside

Rotating outer
cylinder

$h = 36.98$ cm

Observation
ports

Test
cylinder

Fixed guard
cylinders

Fluid injection
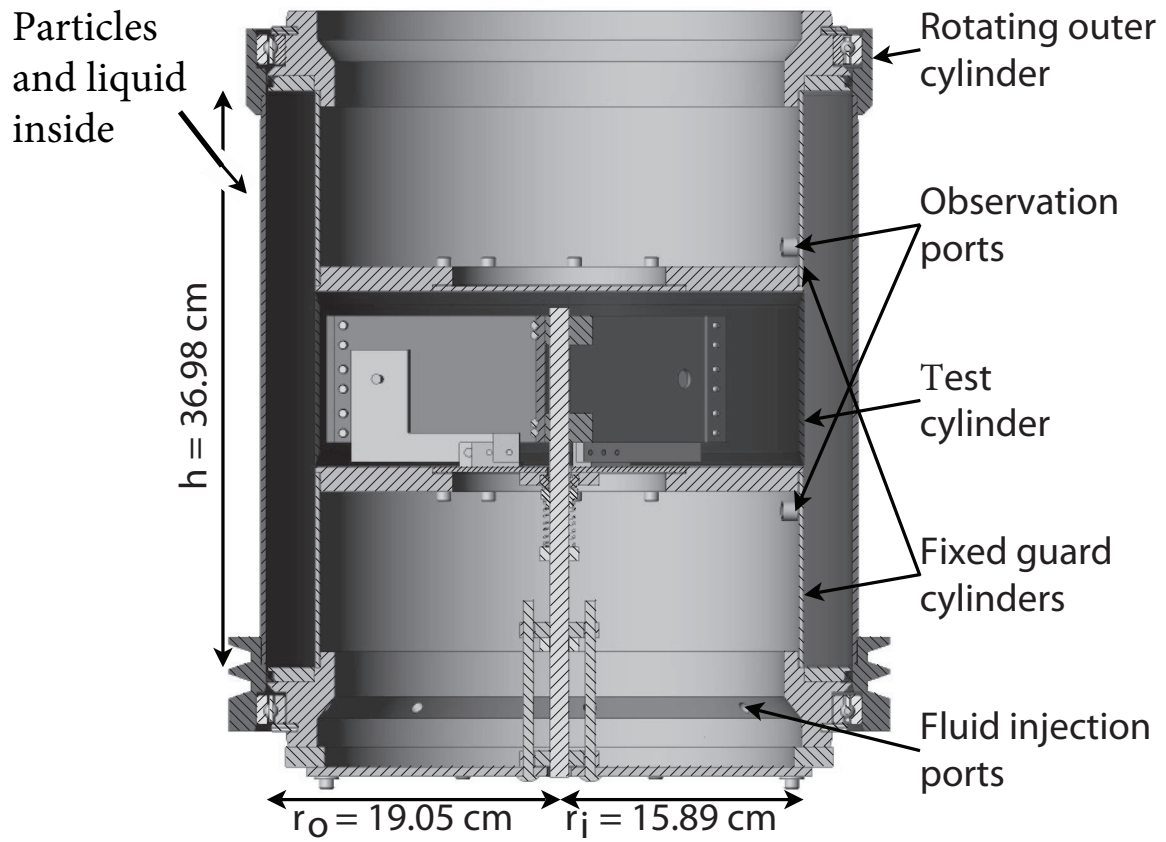ports

$r_o = 19.05$ cm $r_i = 15.89$ cm

Figure 2.1: Rheometer, Couette flow device. The liquid-solid mixture is sheared by the rotation of the outer cylinder. The top and bottom cylinders are fixed. The inner middle cylinder (test cylinder) is free to rotate slightly so as to measure the torques created by the flow.

Property	Smooth walls	Rough walls
Annulus height (h_T)	36.98 cm	36.98 cm
Test cylinder height	11.22 cm	11.22 cm
Fixed guards height	12.7 cm	12.7 cm
Annulus inner radius (r_i)	15.89 cm	16.22 cm
Annulus outer radius (r_o)	19.05 cm	18.72 cm
Annulus gap (b)	3.16 cm	2.49 cm
Ratio of height to gap (h_T/b)	11.7	14.84
Ratio of gap to outer radius (b/r_o)	0.166	0.133
Maximum rotational speed (ω)	14.9 rad s^{-1}	14.9 rad s^{-1}
Re critical	1.6×10^4	1.1×10^4

Table 2.1: Rheometer properties and dimensions

fixed guards and the central shaft are equipped with seals that prevent the fluid from entering the bearings. The fixed guard cylinders are separated from the test cylinder by a knife edge gap (0.7 mm) to prevent the particles from exiting the annulus gap but allowing the test cylinder to rotate freely. The height of the test cylinder, H, is 11.22 cm, the inner radius of the annulus, r_i, is 15.89 cm, the outer radius of the annulus, r_o, is 19.05 cm, and the width of the annulus between the cylinders when the walls are smooth, b, is 3.16 cm. The outer cylinder is driven by a belt connected to a motor; the maximum rotational speed is $\omega = 14.8$ rad s^{-1}. Hence, the maximum shear rate, $\dot{\gamma} = 2\omega r_o^2/(r_o^2 - r_i^2)$, is 123 s^{-1}. The experiment dimensions and its range of speeds are listed in Table 2.1. Mechanical drawings of the rheometer parts can be found in the thesis of Koos (2009). To avoid slip at the wall, the inner and outer cylinder walls are roughened by coating them with polystyrene particles. The particles are glued to thin waterproof vinyl sticker sheets (commonly used as aquarium backgrounds), which covered both surfaces. The glued particles are oriented randomly and have a surface area fraction of 0.70. The decrease in gap thickness due to the rough walls is considered when calculating the shear rate and the change in dimensions is reported in table 2.1.

Shearing the mixture by rotating the outer cylinder is preferred over shearing it by rotating the inner one because Taylor vortices develop at lower rotational speeds in the latter case due to centripetal forces (Taylor, 1936a,b; Wendt, 1933). Besides delaying the presence of secondary flows by rotating the outer cylinder, the rheological measurements are made away from the top and bottom boundary where the secondary flows develop. The contribution to the measured torque by end effects is attenuated by increasing the ratio of height and shearing gap width, ($H/b = 11.7$). Further delay

is achieved through the increase in the ratio of gap width to outer radius (b/r_o). By using a modified gap Reynolds number ($Re_b^* = \rho r_o \omega b / \mu$, where ω is the angular velocity of the outer cylinder), it is possible to determine the critical Re_b^* at which these secondary flows occur (Taylor, 1936a,b). Using the data of Taylor, a critical modified gap Reynolds number of 1.6×10^4 is found for this apparatus when the walls are smooth and 1.1×10^4 when the reduction in gap width due to added roughness is considered. The modified gap Reynolds number range for a pure fluid (no particles) in the current experiments is $1.0 \times 10^3 \leq Re_b^* \leq 7.2 \times 10^4$, and thus some of the experiments are above the critical Reynolds number; however, the presence of solid particles increases the effective viscosity of the flow and hence decreases the Reynolds number.

2.2 Torque measurements

Unlike Bagnold (1954), in which the torque was not measured directly, the torque measurements in this work are directly taken in the test section located in the middle of the inner cylinder (see Figure 2.1) without removing any possible contribution to friction or fluid. The test cylinder is allowed to deflect rotationally due to the torque applied by the flow. The rotation of the test cylinder is opposed by a linear spring that is connected to a static reference. The spring connects to the test cylinder through a torque arm. The torque is measured by measuring the elongation of the spring. Different springs with different stiffness are used depending on the torque applied by the flow. To overcome the spring initial tension every spring is preloaded. A pulley is used to direct the preload and reduce friction. An optical probe and a fotonic sensor (MTI 0623H and MTI KD-300, respectively) is mounted on a static reference to measure the spring displacement. The arm that connects the test cylinder to the spring is equipped with a mirror that is used as the moving target for the optic probe. A sketch of the torque measurement setup is shown in Figure 2.2. The calibrations of the optical probe and the springs are discussed in Subsection 2.2 and 2.2, respectively, followed by the methodology for measuring the rheometer angular speed.

Optical probe calibration

The optical probe contains a set of light transmitting and light receiving fibers that are aligned in a hemispherical configuration. Light is fed to the transmit fibers, where it exits the probe tip and hits the target. Light that is reflected from the target is captured by the receive fibers and transmitted to the fotonic sensor that converts the light intensity to voltage. The output voltage is proportional to the distance between the probe tip and the target being monitored. Figure 2.3 shows a diagram of the fotonic sensor output as a function of target displacement. When the target is in contact with the optic probe, no light is received by the fibers, giving an output signal of zero. The voltage increases with increasing distance reaching a maximum. Past the optical peak, there is
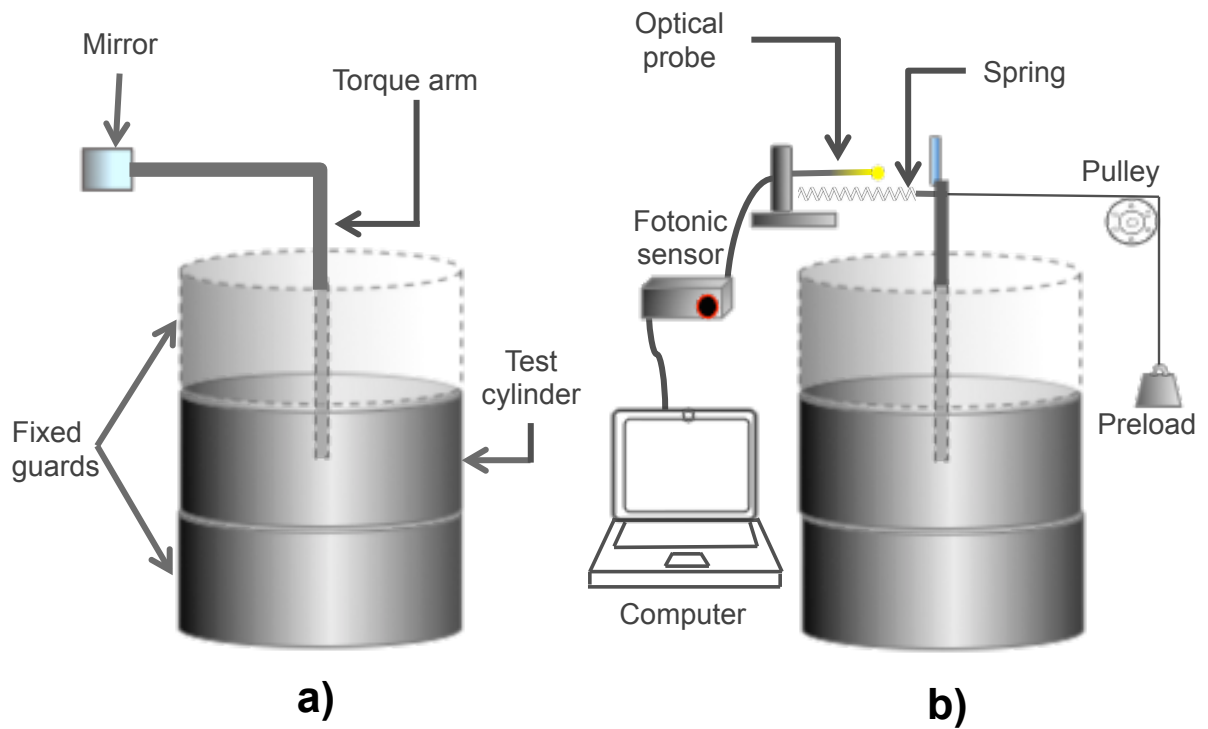
Figure 2.2: Torque measurement system. The outer rotating cylinder is left out of the drawing for clarity. (a) Front view of inner cylinder. The mirror attached to the torque arm is the target monitored by the optical probe. (b) Side view of the inner cylinder. The optical probe and the spring are attached to a stationary frame. The spring is connected to the test cylinder through the torque arm. The signal from the fotonic sensor is read out and stored in the computer.

a sensitive linear output response (Range 2). The optical probe is positioned far enough from the moving target to make sure that the sensor output is in this range. The optical probe sensitivity post the optical peak is 30 $\mu m/mV$. The optical probe is calibrated using a dial gage. A typical calibration curve is shown in Figure 2.4. The curve that best fits the data is a rational polynomial and its coefficients depend on the initial target position. The optical probe is calibrated prior to every set of experiments and when a spring is changed. This calibration is repeated at least 10 times and the final calibration curve is the average of these calibration curves. The fotonic sensor records the optical probe signal for 10 seconds with a frequency sample of 10,000 Hz. The sensor output is then averaged and coverted it to displacement using the calibration curve.
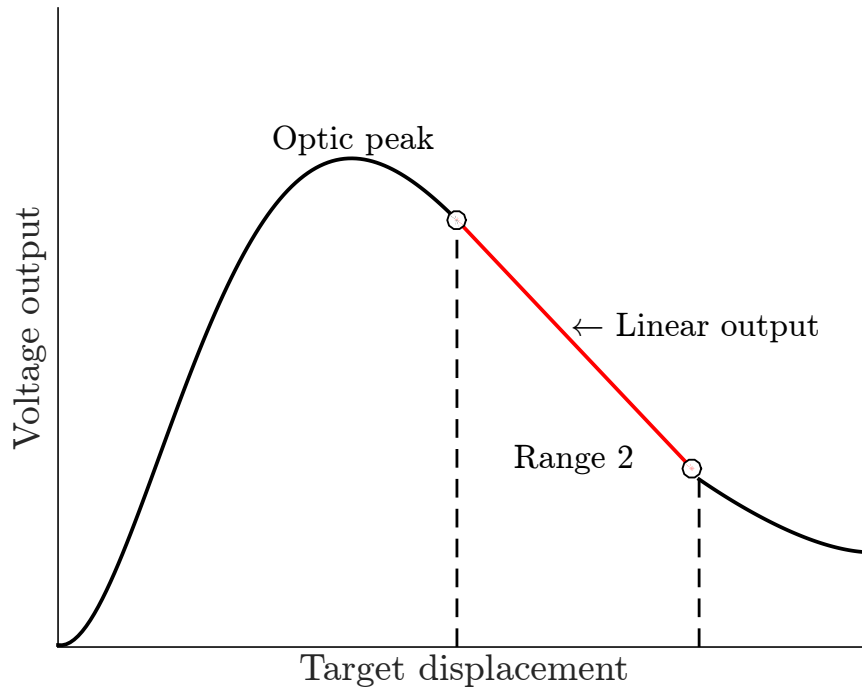

Figure 2.3: Diagram of an MTI KD-300 fotonic sensor output as a function of target displacement.

Springs calibration

The springs used to measure the torque were manufactured by *Century springs*. The calibration of the spring is carried out by loading the spring with known masses. The masses are weighted prior to each calibration using a scale with a resolution of 0.05 grams. The masses are attached to the torque arm through a fishing line that runs through a pulley (see Figure 2.2). The torque arm is connected to the spring and hence the spring can be loaded and its displacement measured for different masses. Springs with different stiffness are used to allow a range of torques (M) between $1.3 \times 10^{-3} \leq M \leq 2.7$ Nm to be measured. The calibration curves for all of the springs used are shown in Figure 2.5. The spring calibration is performed while the rheometer is filled with
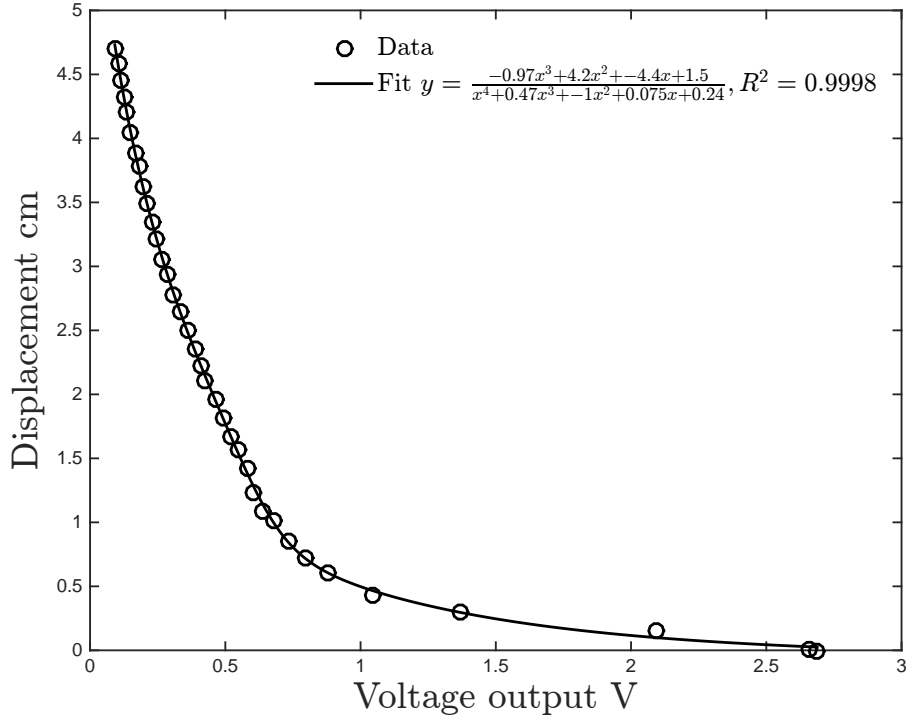
Figure 2.4: An example of a fotonic sensor calibration curve. All the calibration curves are best fitted by a rational polynomial. The order of the polynomial numerator and denominator is 3 and 4, respectively.

water and running at different speeds. Each point represents the mean of at least 15 individually recorded measurements; the error bars represent the standard deviation in these measurements. The R-squared average for all the linear fits is 0.999. The lowest R-squared corresponds to the spring with the highest slopes (and equivalently with the highest sensitivity). An initial torque is required to start the displacement of the spring; this torque is given by the x-intercept of the calibration curve. All the experiments are preloaded with the corresponding spring initial torque to guarantee maximum sensitivity. The calibration curve for the spring with the highest resolution and sensitivity is shown in Figure 2.6. The initial torque has been subtracted to show the maximum resolution of this spring. A maximum deviation from the linear fit of 17% occurs at the lowest torques applied. The R-squared value of this fit is 0.9988.

During the torque measurements, the displacement of the spring is also recorded with a digital camera to account for any possible mis-calibration of the optical probe. The photos taken of the spring are used to measure its displacement and double check the sensor output.

Angular speed measurements

The rotation of the outer cylinder is measured using a magnetic sensor and a laser tachometer. The two devices are used to account for uncertainties in the speed measurements. For the lowest
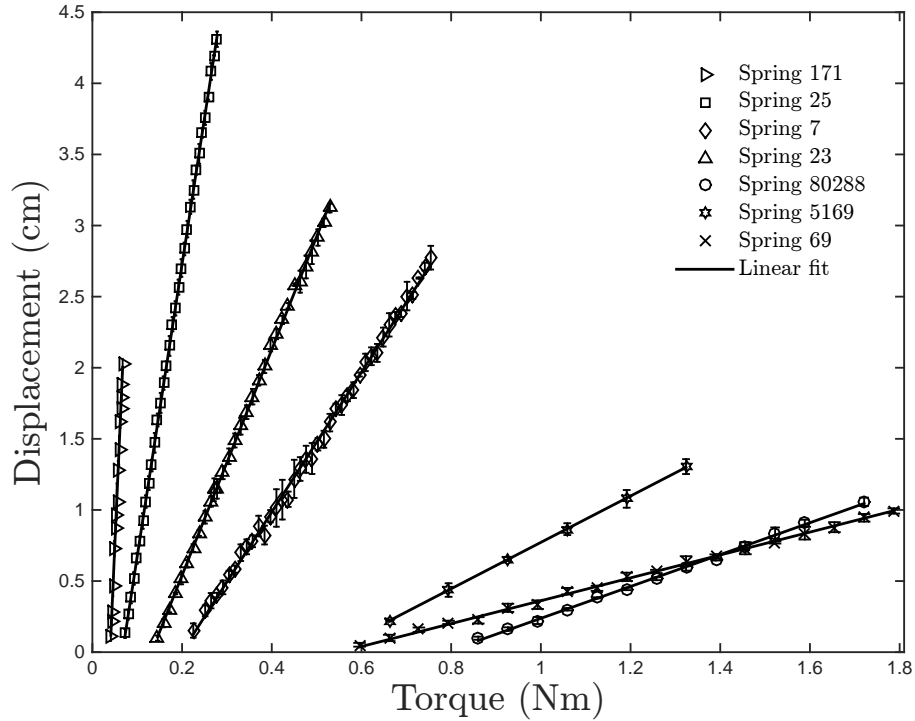
Figure 2.5: Springs calibration curves. The spring constant and its sensitivity are given by the slope of the linear fit. The error bars correspond to the standard deviation of the measurements.
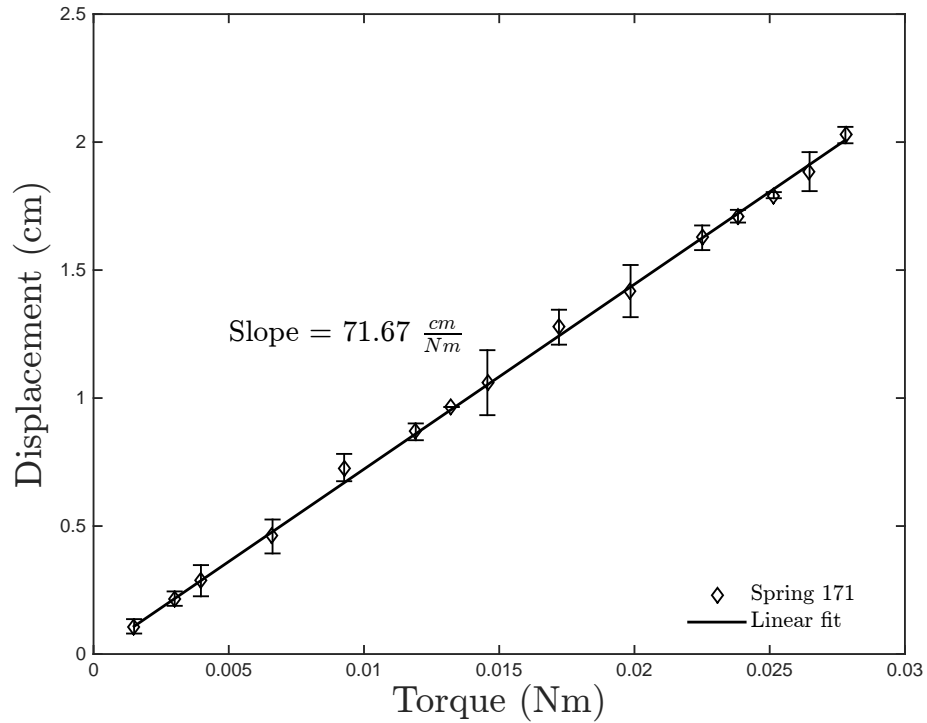

Figure 2.6: Calibration curve for spring 171-b (highest sensitivity). The spring constant and its sensitivity are given by the slope of the linear fit. The error bars correspond to the standard deviation.

rotational speeds, a chronometer is also used to account for the reduction of accuracy of the laser tachometer. The magnetic sensor does not work for rotational speeds below 2.87 rad s^{-1}. To increase the accuracy of the laser tachometer at low speeds, 8 reflective marks were evenly spaced and placed on the outer cylinder. Due to the high reflectiveness of stainless steel, the laser is pointed to a black stripe painted on the outer cylinder where the reflective marks are located. Figure 2.7 shows a sketch of the rotational speed measurement system. In the previous work of Koos (2009),
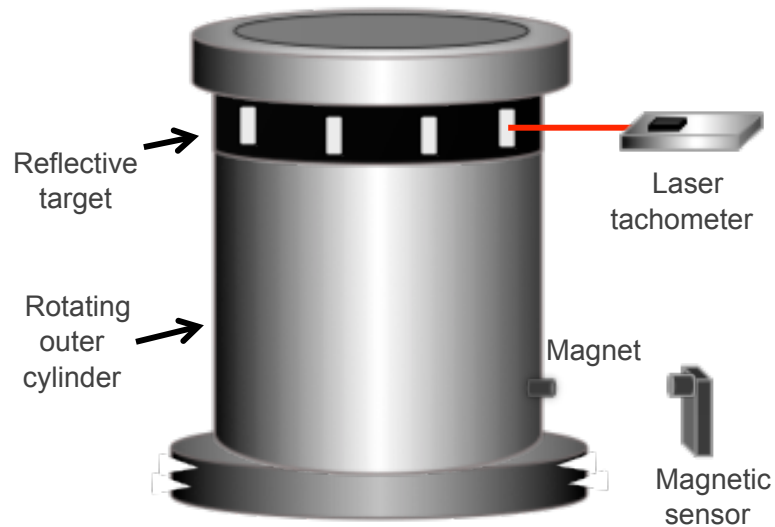

Figure 2.7: Sketch of the rotational speed measurement system. The rotational speed is measured with a laser tachometer and a magnetic sensor.

the angular speed was measured by counting the outer cylinder revolutions and measuring the time with a chronometer. Measurements of the angular speed using this method were performed while measuring the angular speed with the laser and magnet sensor to measure the uncertainty on the previous speed measurements. The outer cylinder is driven by a belt connected to a motor; the motor speeds are controlled via a Bardac drive that allows the gradual increase of the speed. To test that the rheometer runs at a constant speed, rotational speed measurements for the laser, magnet sensor, and chronometer were recorded for a period of 1.5 hours for 9 different speeds. Figure 2.8 shows the rotational speed measurements for each instrument. The measurements are in good agreement; the highest deviation is found at the highest rotational speeds for the measurements that used the chronometer. The outer cylinder angular speed is shown to maintain a constant speed for all the different speeds tested. Figure 2.9 shows the measured angular speed for each control speed tested. Each point represents the mean of all the measurements taken from the 3 instruments. Even when the chronometer method exhibits the biggest deviation, this deviation is no larger than 6% of the average speed measured using the laser tachometer. Hence, the maximum uncertainty in the speed measurements from the previous work of Koos (2009) is less than 6%.
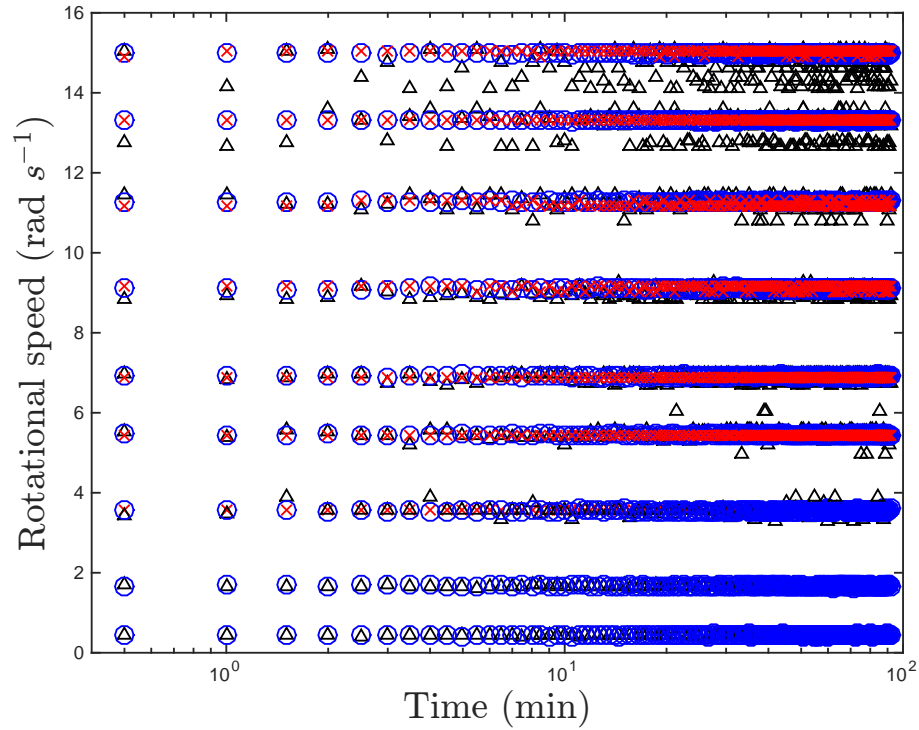
Figure 2.8: Measured rotational speed as a function of time for each measurement device. x , ◯ and △ symbols correspond to the rotational speed measurements used using the magnetic sensor, laser tachometer, and chronometer, respectively.
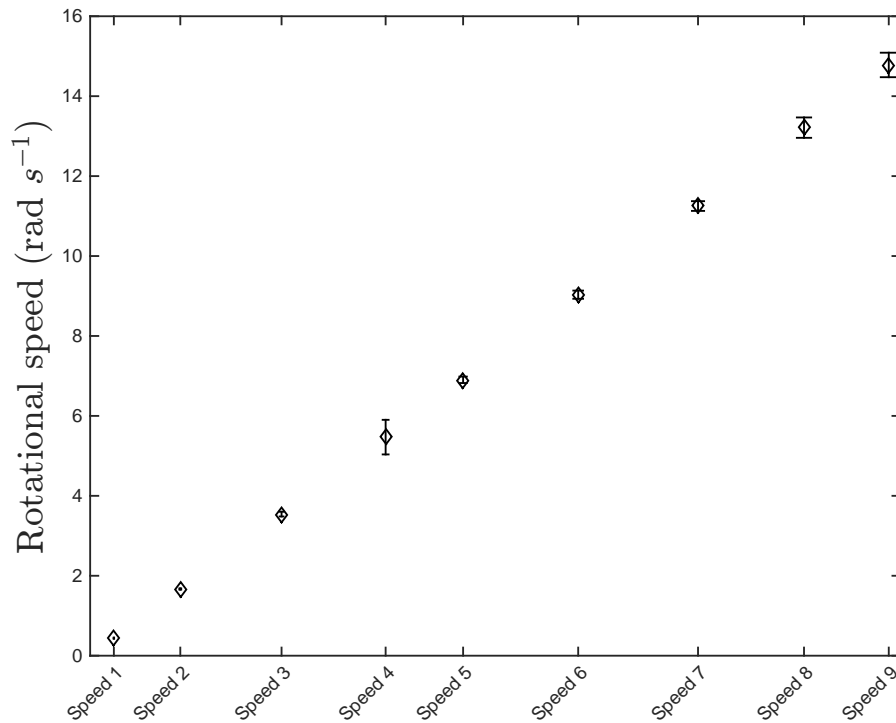

Figure 2.9: The mean rotational speed measured with the three different instruments as a function of the motor speed tested. The error bars represent the standard deviation in these measurements.

2.3 Error analysis

The uncertainty contributions considered for the torque measurements are:

- Uncertainty in spring constant measurement

- Uncertainty in distance measurement

- Uncertainty in optical probe calibration curve

A set of several repeated readings has been taken for each contribution. The mean and standard deviation are calculated for each set. The estimated standard uncertainty for each contribution is calculated as follows:

$$u = \frac{\sigma}{\sqrt{n}}, \tag{2.1}$$

where u is the standard uncertainty of the measurement, σ is the standard deviation, and n is the number of measurements. Each individual standard uncertainty is then combined in terms of relative uncertainty . The combined uncertainty is given in root mean squared (RMS) of each individual uncertainty terms,

$$u_T = \sqrt{\left(\frac{u(K)}{K}\right)^2 + \left(\frac{u(D)}{D}\right)^2 + \left(\frac{u(V)}{V}\right)^2} \tag{2.2}$$

where $u(K)$, $u(D)$, and $u(V)$ are the standard uncertainty of the spring constant, distance, and optical probe calibration, respectively. As mentioned in Subsection 2.2, the calibration curve of the optical probe used for each experiment is the mean of at least 10 curves obtained prior to each experiment. The distance uncertainty corresponds to the spring elongation measurements performed to measure the torque of the flow. At least five torque measurements are taken for each speed tested. To estimate the spring constant uncertainty, at least ten measurements of the calibration curves are considered for each spring. The uncertainty of the rotational speed is estimated as the standard deviation in the speed measurements. Both the laser tachometer and the magnet sensor are used to record the outer cylinder speed for each torque measurement. The change in suspending liquid temperature is recorded thoughout the duration of the experiments. The variation in temperature and consequently the variation in suspending liquid density and viscosity, contributes to the uncertainty in Stokes and Reynolds number (u_{St}, u_{Re}). For these dimensionless numbers the combined uncertainty is given by

$$u_{St} = u_{Re} = \sqrt{\left(\frac{u(\omega)}{\omega}\right)^2 + \left(\frac{u(\mu)}{\mu}\right)^2 + \left(\frac{u(\rho)}{\rho}\right)^2}, \tag{2.3}$$

where $u(\omega)$, $u(\mu)$, and $u(\rho)$ are the standard uncertainty of the rotational speed, viscosity, and density of the liquid, respectively.

2.4   Pure fluid torque measurements

To test the experimental method, torque measurements are performed for an aqueous-glycerine mixture with no particles and plain water. These measurements are taken with rough walls. The temperature of the fluid and density are monitored and considered when calculating the fluid properties. The range of gap Reynolds number tested is $3.6 \times 10^2 \leq Re_b \leq 8.3 \times 10^4$. The torque measurements are compared with the theoretical results for Couette flow. Considering an infinitely long cylindrical Couette device with the outer cylinder rotating and the inner cylinder being held stationary, the torque applied by a laminar flow to the inner cylinder considering smooth walls is (Schlichting, 1951)

$$M_i = -M_o = 4\pi\mu H \frac{\dot{\omega} r_i^2 r_o^2}{r_o^2 - r_i^2} = M_{laminar}, \qquad (2.4)$$

where H is the height of the test cylinder, μ and ρ are the viscosity and density of the fluid, respectively, and r_i and r_o are the inner and outer cylinder radius. The decrease in gap thickness due to the rough walls have been taken into account for the values of r_i and r_o. The effect of rough walls is discussed later in this section. Figure 2.10 shows the torque as a function of the shear rate for a 77% and 21% in volume aqueous-glycerine mixture and for plain water. Each point represents the mean of 10 individually recorded measurements; the vertical error bars represent the combined torque uncertainty. The uncertainty of the shear rate is represented by the horizontal error bars. The theoretical results for Couette flow are also shown in Figure 2.10. For an aqueous glycerine mixture of 77%, the torque measurements are in good agreement with the theoretical laminar Couette solution. The maximum deviation from the laminar solution is 14%. For the lower glycerine percentage of 21% and plain water, the measured torques do not compare favorably with the torques corresponding to laminar flow theory. For both liquids the measured torques are considerably higher than the one predicted for laminar flow. The measured torques for water are very close in value to the ones measured for the 21% aqueous-glycerine mixture, even though the aqueous glycerine mixture is 1.8 times more viscous than water.

Figure 2.11 shows the measured torques normalized by the theoretical torque as a function of the gap Reynolds number defined as

$$Re_b = \frac{\rho \dot{\gamma} b^2}{\mu} \qquad (2.5)$$

The reduction in shear gap width due to the rough walls has been considered when calculating the gap Reynolds number. For the case with the highest percentage of glycerine (and thus the lower gap Re range), the normalized torque is close to one. The maximum uncertainty for this case occurs at the lowest gap Reynolds number. For the case of 21% of glycerine, the normalized torque is between 4 and 15 times higher than the theoretical torque, while the normalized torque for water is between 9 and 29 times higher.
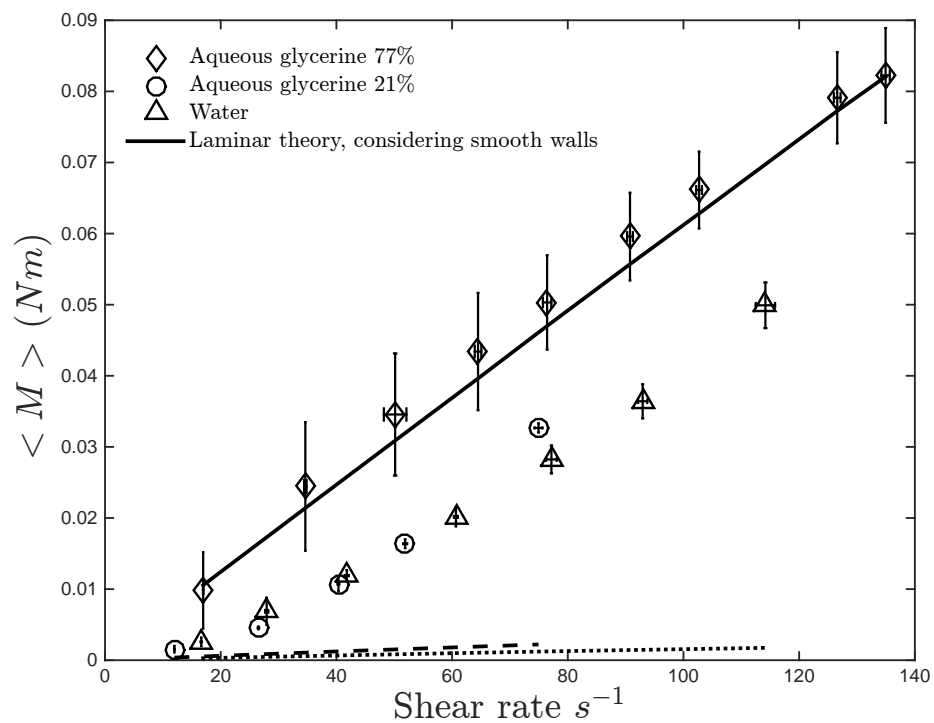
Figure 2.10: Measured torque as a function of the shear rate for an aqueous-glycerine mixture with no particles. The percentage in volume of glycerine is 77% and 21% for the aqueous-glycerine mixtures. The lines correspond to the theoretical Couette solution for a laminar flow with a viscosity corresponding to the liquid at the recorded temperatures. Continuous and dash lines correspond to 77% and 21% aqueous glycerine. Dotted line is the theoretical torque for plain water.
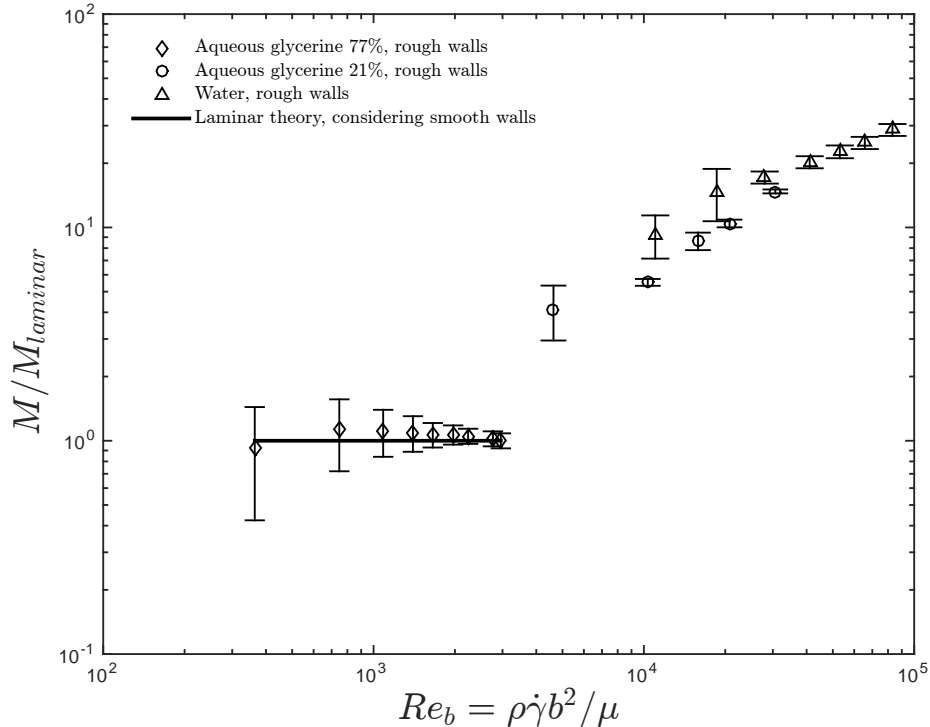
Figure 2.11: Normalized torque as a function of the gap Reynolds number for an aqueous-glycerine mixture of 77% and 21% and plain water with no particles.

To compare the current results with the work of Taylor (1936a), Figure 2.12 shows the normalized torques as a function of the modified gap Reynolds number used by Taylor, defined as

$$Re_b^* = \frac{\rho \omega r_o b}{\mu}. \tag{2.6}$$

Based on the work of Taylor (1936a,b) and considering the reduction in gap due to the rough walls, the critical gap Reynolds number at which the flow becomes unstable for the current apparatus geometry is 1.1×10^4 (for rough walls). The range of gap Reynolds number corresponding to plain water and 21% aqueous glycerine is between $4.6 \times 10^3 \leq Re \leq 8.31 \times 10^4$. Therefore, most of these experiments are above the critical Reynolds number. Figure 2.12 also shows the normalized torques from Koos (2009) performed with smooth walls. Comparing the smooth and rough walls measurements, the ratio of torques for the latter deviates from the laminar behavior at modified gap Reynolds where the smooth walls show laminar behavior. This suggests that the presence of rough walls can lower the critical Reynolds number.

Figure 2.13 shows a comparison between the current measurements and the data of Bagnold (1954); Taylor (1936a) and Wendt (1933) for pure fluid torque measurements normalized with the torque predicted from laminar theory. The normalized torques are presented as a function of the modified gap Reynolds number (Re_b^*) used by Taylor (1936a) and defined as equation 2.6. All of
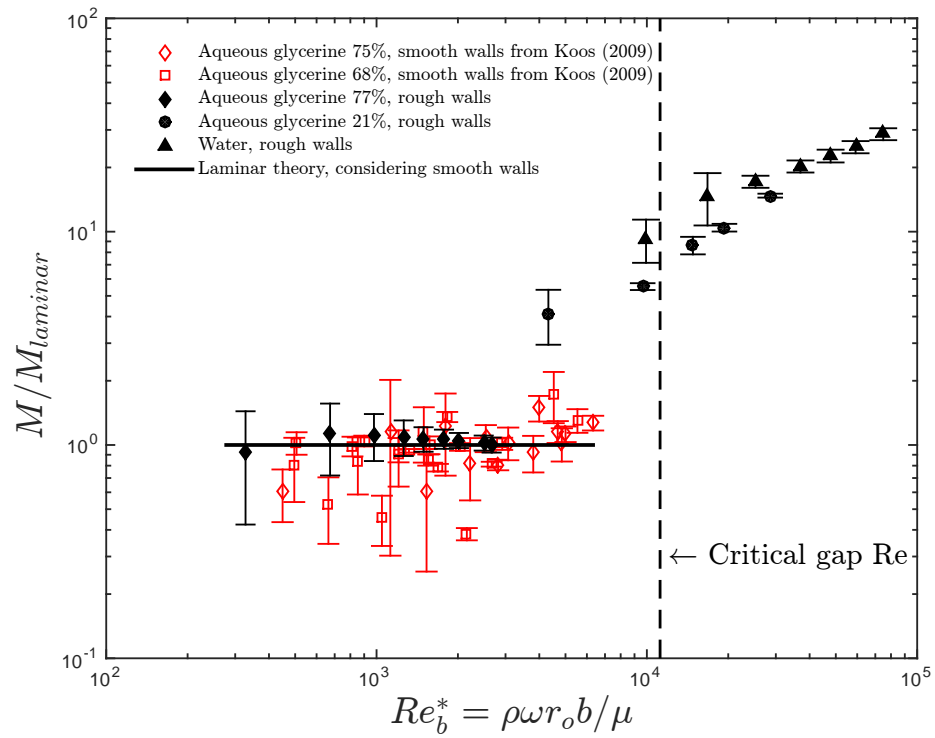
Figure 2.12: Closed symbols: normalized torques as a function of the modified gap Reynolds number for pure fluids measured with rough walls. Open symbols: normalized torques for pure fluid measured with smooth walls from Koos (2009). Vertical dashed line represents the critical modified Re based on the work of Taylor (1936a) and considers the gap width for rough walls.

these studies were performed with smooth walls. The shear gap width to outer radius ratio for the current experiments is smaller ($b/r_o = .133$) than the corresponding ratio for the data of Taylor ($b/r_o = .15$ and $b/r_o = .21$), Wendt ($b/r_o = .15$), and Bagnold ($b/r_o=.19$). A smaller ratio leads to lower critical gap Reynolds number. The normalized torques for the lower range of gap Re compares favorably with the current results; however, a deviation from laminar theory occurs at a lower Reynolds number than the one predicted using the data of Taylor (1936a). Cadot et al. (1997); Lee et al. (2009) and van den Berg et al. (2003) studied the effect of rough boundaries on Taylor-Couette flow, where the liquid was sheared by the rotation of the inner cylinder. These studies show that the presence of rough walls does not affect the laminar transition. A lower critical Re might be due to a smaller ratio in the annulus height to shear gap width. For the experiments of Taylor, this ratio was $h_T/b = 99$ and $h_T/b = 141$, and for the experiments of Wendt, $h_T/b = 28$, which is considerably higher than the ratio for the current experiments ($h_T/b = 14.9$). Moreover, when the flow is driven by the rotation of the outer cylinder, Taylor (1936a) observed that the transition occurred at a range of Reynolds number rather than at an specific one. Experiments on Taylor-Couette flow with rough walls and inner cylinder rotating indicate that the presence of rough walls does not affect the instability of Taylor vortex flow for low Reynolds numbers, but it does intensify the turbulent Taylor vortex flow at Reynolds numbers above the critical one (Lee et al., 2009). This rough walls effect leads to higher measured torques. The measured torque for pure fluid for the current experiments is consistent with these findings.

To verify the Newtonian behavior of the liquids used for these experiments, viscosity measurements were performed using a strain-controlled rheometer (TA instruments, ARES-RFS, Rheometrics fluid Spectrometer). The results obtained using the rheometric fluid spectrometer indicate that the liquids used are indeed Newtonian.

2.5 Particles

Two type of particles are used in these experiments: polystyrene elliptical cylinders and polyester scalene ellipsoids. The properties of these particles are summarized in table 2.2. The diameter reported in table 2.2 is the equivalent spherical particle diameter. These particles are the same particles used by Koos et al. (2012). The particles vary in size, shape, and density. These variations lead to different values for the random loose and random-close packing. The values used for these packings were obtained from the measurements done by Koos (2009).

Polystyrene: density ratio = 1 and 1.05

Figure 2.14 shows the polystyrene particles used in the current experiments, which are elliptical cylinders. The specific gravity for these particles is 1.05 and they are neutrally buoyant in an aqueous
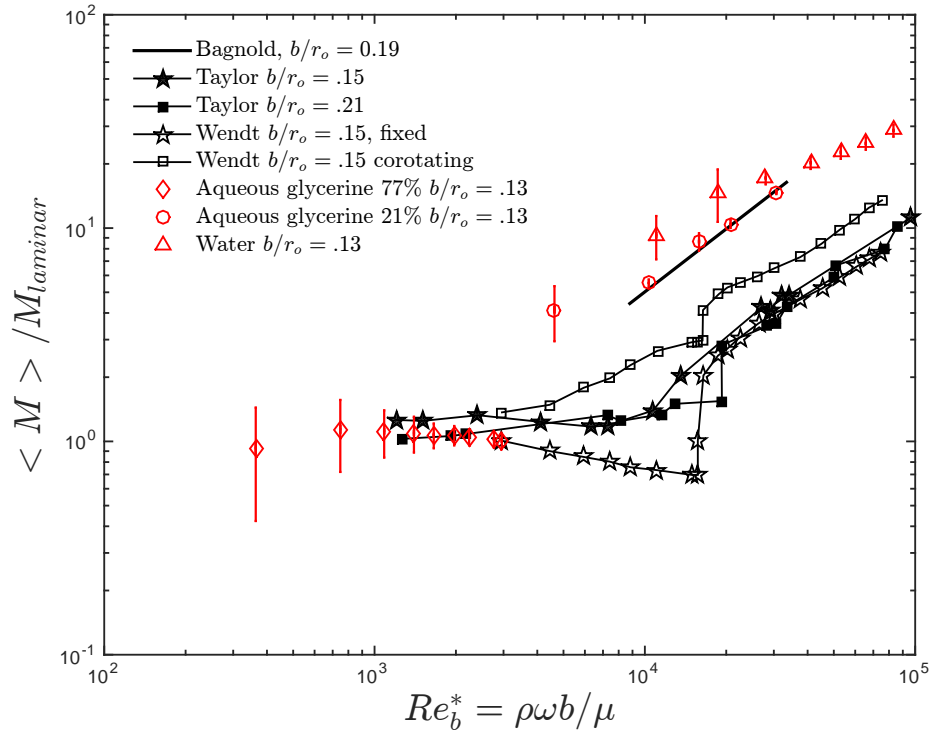
Figure 2.13: Pure fluid torque measurements normalized with laminar Couette flow as a function of modified gap Reynolds number. Comparison between pure fluid data of Bagnold (1954); Taylor (1936a) and Wendt (1933).

Property	Polystyrene	Polyester
diameter, d (mm)	3.34	2.93
$\dfrac{\text{gap width smooth walls}}{\text{diameter}}$, b_s/d	9.46	10.79
$\dfrac{\text{gap width rough walls}}{\text{diameter}}$, b/d	7.46	8.5
particle density, ρ_p (kg/m^3)	1050	1400
liquid density, ρ (kg/m^3)	1000-1050	1000-1160.5
shape	elliptical cylinders	ellipsoids
sphericity, ψ	0.7571	0.9910
RLP, ϕ_{RLP}	0.553	0.593
RCP, ϕ_{RCP}	0.663	0.65
Young's modulus, E (MPa)	3000	2800
Yield Strength, Y (MPA)	40	55
Poisson's ratio ν	0.34	0.39

Table 2.2: Particles properties

glycerine mixture of 21% glycerine. Koos (2009) measured the particle diameter and lengths of 50 particles. The sample had an average small diameter $d_{small} = 2.08$ mm, large diameter $d_{large} = 2.92$, and length $l = 3.99$ mm. The particle length was found to be bimodal, whereas the diameters were found to be unimodal. By measuring the displaced volume of 1000 particles and considering that the volume of each particle is

$$V_p = \frac{\pi}{4} d_{small} d_{large} l.$$

Koos (2009) found an equivalent sphere diameter of $d = 3.35$ mm. By weighing the same sample and considering a particle density of $\rho_p = 1050 \ kg/m^3$, an equivalent sphere diameter of $d = 3.34$ was found. Both measurements were in agreement and the particles are taken to have an equivalent spherical diameter of $d = 3.34 \pm 0.02$ mm. Polystyrene particles are the ones used to roughen the
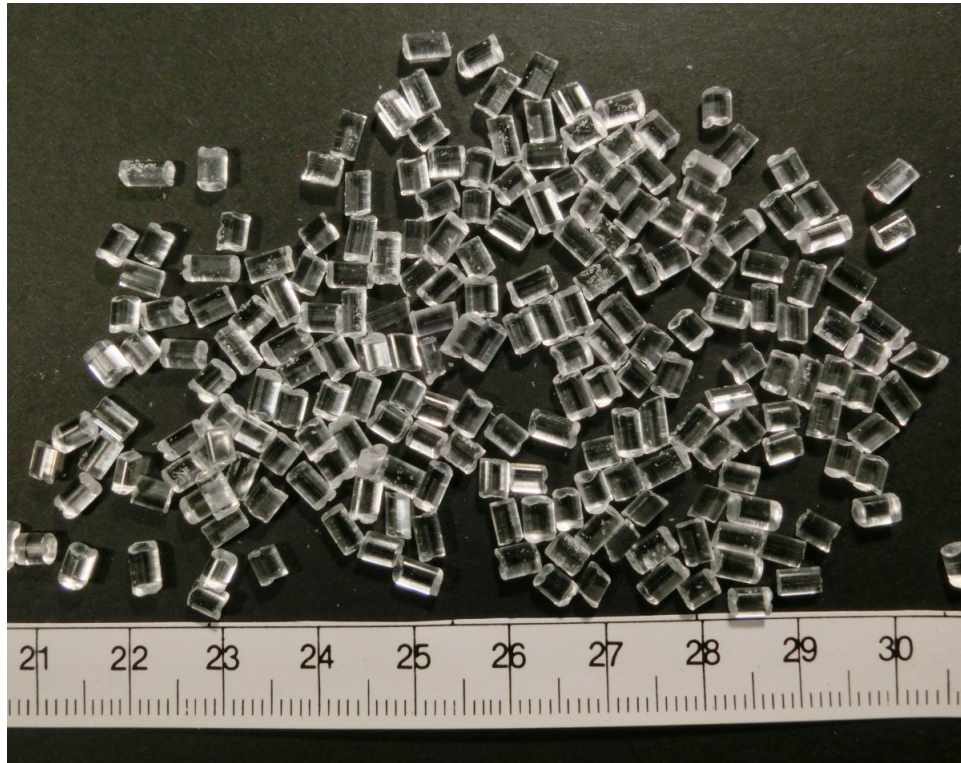
Figure 2.14: Polystyrene particles. Specific gravity of 1.05 and have an equivalent spherical particle diameter of 3.34 ± 0.02 mm. Reference shown in cm.

rheometer walls. Figure 2.15 shows a picture of the surface roughness of the walls using polystyrene particles.

Polyester: density ratio=1.2 and 1.4

The polyester particles used in the current experiments are shown in Figure 2.16. These particles have a specific gravity of 1.4 and a shape of scalene ellipsoids. Koos (2009) found an equivalent
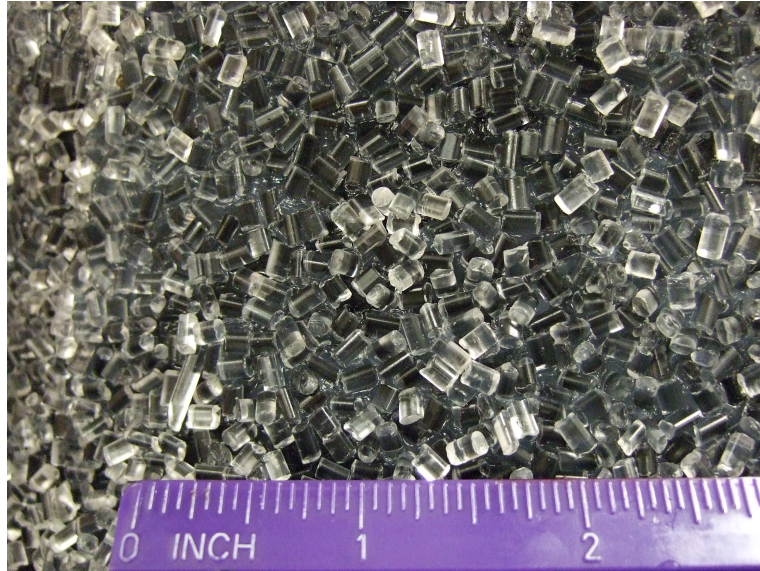
Figure 2.15: Rheometer walls surface roughness formed by polystyrene particles. The reference is in inches.

spherical diameter of $d = 2.93 \pm 0.02$ mm. The rough walls used in these experiments are the same

Figure 2.16: Polyester particles. Specific gravity of 1.4 and have an equivalent spherical particle diameter of 2.93 ± 0.02 mm. Reference shown in cm.

as the ones used for the polystyrene particles.

2.6   Visualizations

Visualizations of the flow are performed by replacing the top fixed guard and test cylinder with a transparent acrylic cylinder. This cylinder has the same radius as the inner cylinder: $r = 15.89$ cm and it is 30 cm in length. The surface of the visualization cylinder is roughened using polystyrene particles. A window of the same length of the cylinder height and 3.8 cm in width is left smooth and used for visualization purposes. Figure 2.17 shows a sketch of the visualization setup. A digital camera is located inside the visualization cylinder to record the flow. The flow is illuminated with halogen lights located on top. An acrylic ring with a width slightly smaller than the gap shear width is put on the rim of the visualization cylinder to work as an end cap. For the visualization of
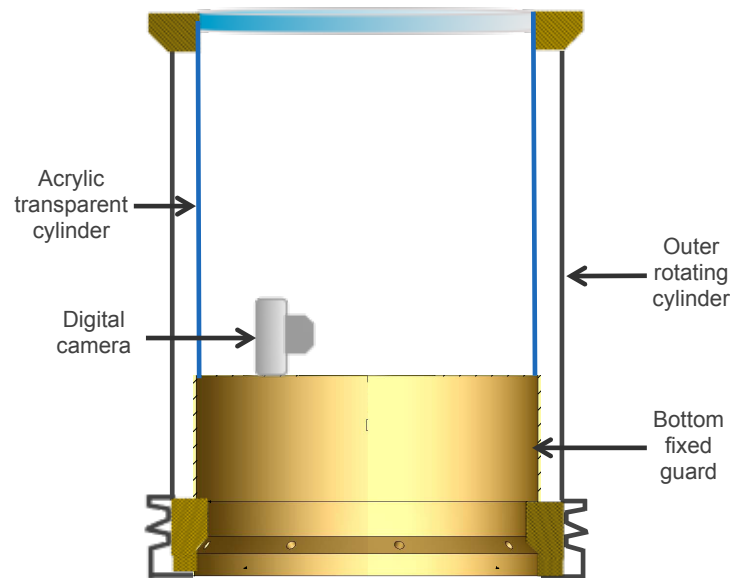

Figure 2.17: Visualization cylinder setup. The walls of the inner transparent cylinder are roughened with polystyrene particles except from the visualization window (3.8×30 cm)

the flow of polystyrene particles, 20% percent of these particles were painted on one side to better track the flow. The painted particles did not exhibit difference in density. Figure 2.18 shows a sample of painted and not painted polystyrene particles immersed in water. The mixture seems to be evenly mixed. Because of the replacement of the test cylinder with the fixed acrylic cylinder, the visualizations of the flow cannot be performed simultaneously with the torque measurements.

Figure 2.18: Sample of polystyrene particles used for visualization purposes. The particles are immersed in water. The mix of painted particles are evenly mixed with the non-painted ones, and thus the paint does not seem to have a considerable influence on particles density.